Structural and Magnetic Studies on Three New Mixed Metal Copper(II) Selenites and Tellurites

Xue-Li Cao, Fang Kong, Zhang-Zhen He, and Jiang-Gao Mao*

Supporting Information

well as heat capacity measured in zero magnetic fields (the inset) for $CdCu(SeO_3)_2$.

Figure S9. Plot of χT versus T for $Hg_2Cu_3(Te_3O_8)_2$.

Table S1. IR data for $CdCu(SeO_3)_2$, $HgCu(SeO_3)_2$ and $Hg_2Cu_3(Te_3O_8)_2$.

	ν(Te/Se-O)	ν(Te/Se-O-Te/Se)
$Hg_2Cu_3(Te_3O_8)_2$	755, 681, 647	509, 443
$HgCu(SeO_3)_2$	796, 717, 671	522, 492, 432
$CdCu(SeO_3)_2$	809, 750, 706	538, 496, 405

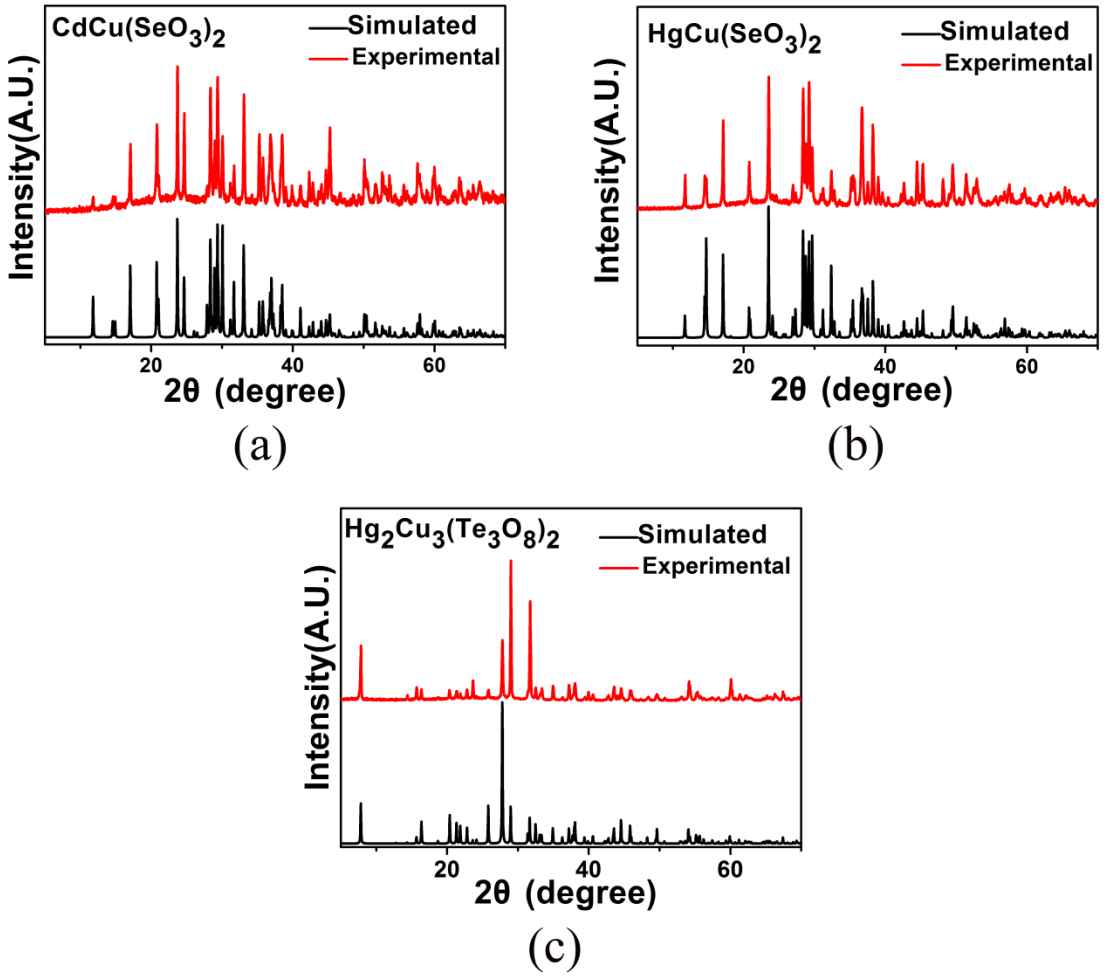

Figure S1. Simulated and experimental XRD powder patterns of $CdCu(SeO_3)_2$ (a), $HgCu(SeO_3)_2$ (b) and $Hg_2Cu_3(Te_3O_8)_2$ (c).

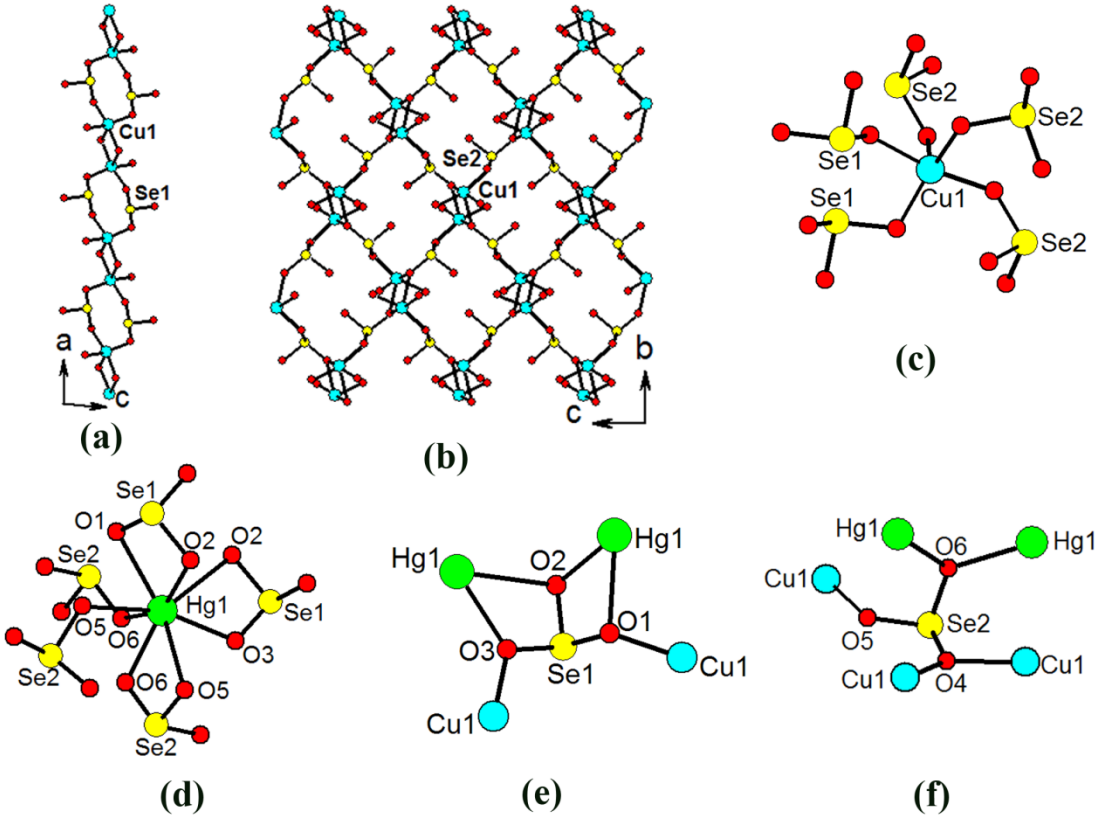

Figure S2. A 1D $[Cu_2O_4(SeO_3)_2]^{8-}$ anionic chain along the *a* axis (a), a 2D $[Cu_2O_6(SeO_3)]^{10-}$ layer parallels to the *bc* plane (b), and the coordination geometries around Cu (c), Hg (d), Se(1) (e) and Se(2) (f) atoms in $Hg_2Cu_3(Te_3O_8)_2$.

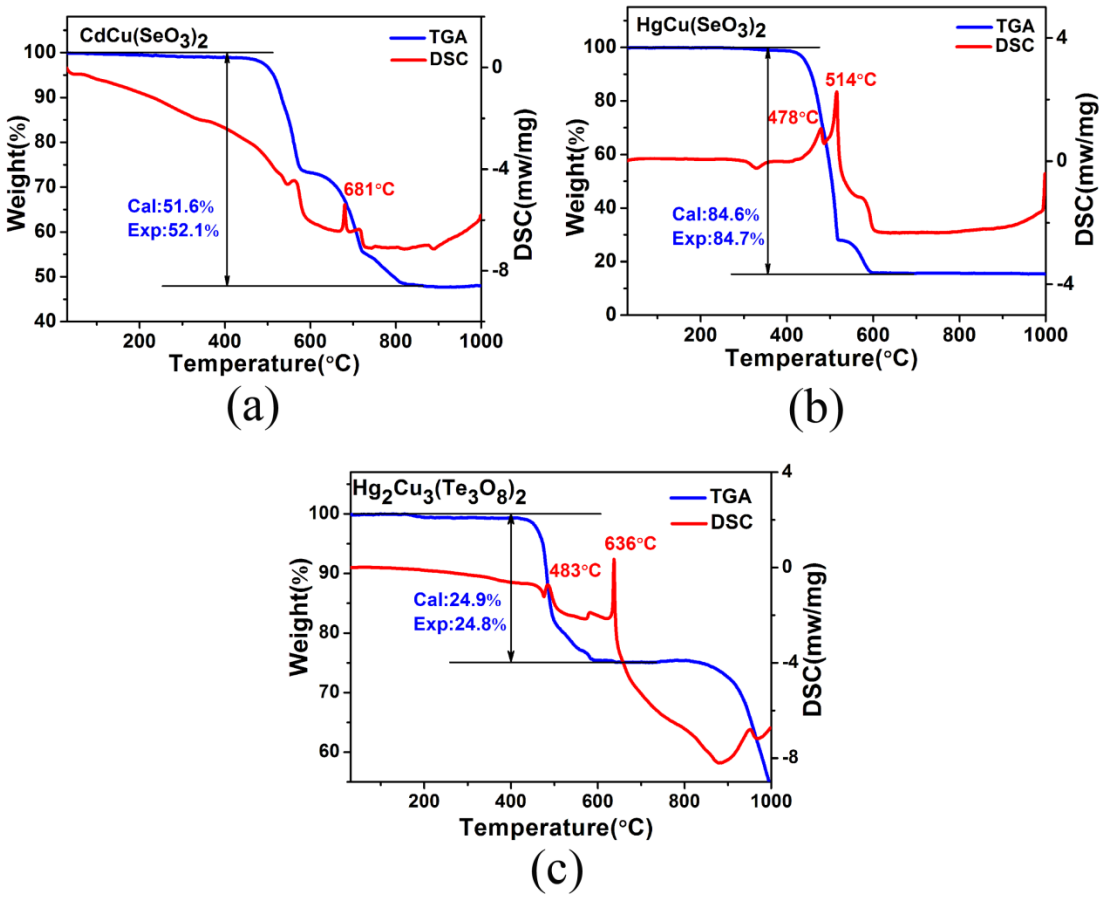

Figure S3. TGA and DSC curves of $CdCu(SeO_3)_2$ (a), $HgCu(SeO_3)_2$ (b) and $Hg_2Cu_3(Te_3O_8)_2$ (c).

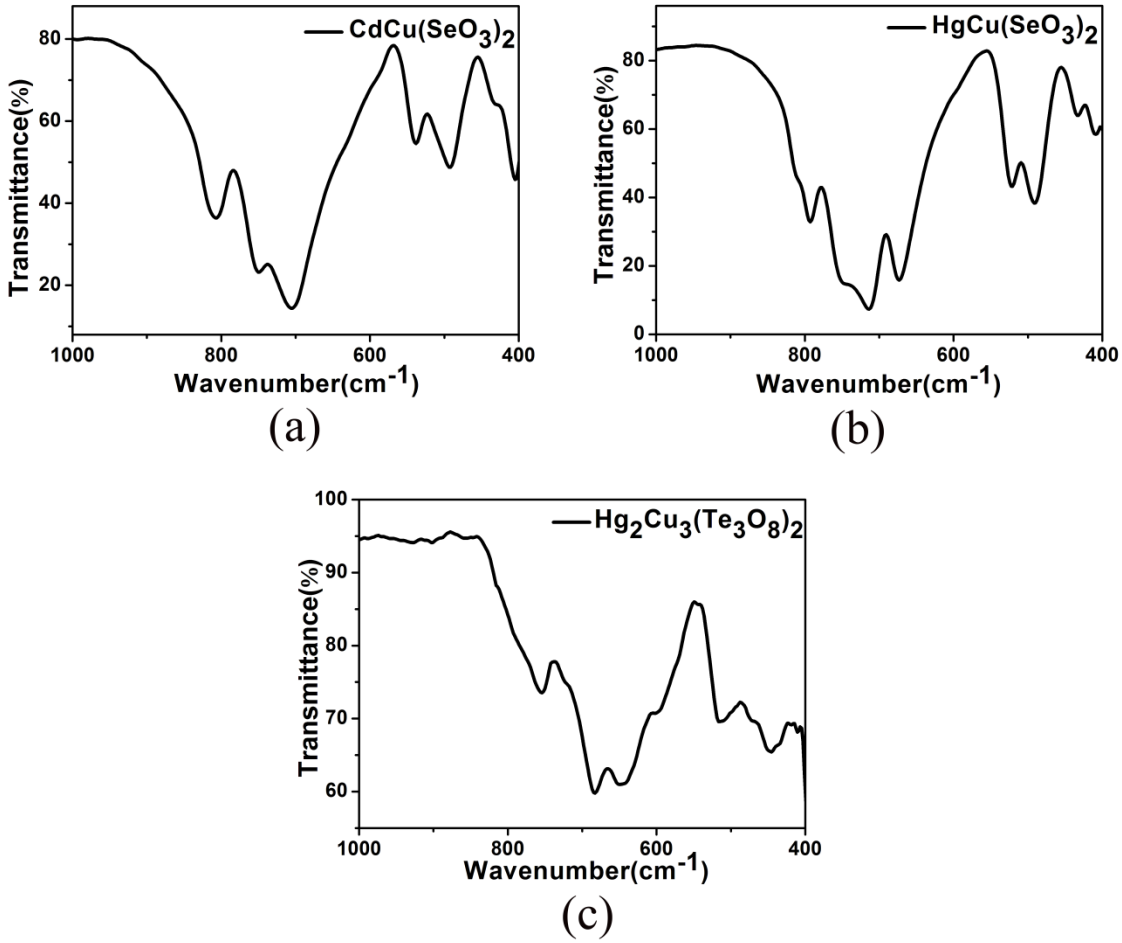

Figure S4. IR spectra of $CdCu(SeO_3)_2$ (a), $HgCu(SeO_3)_2$ (b) and $Hg_2Cu_3(Te_3O_8)_2$ (c).

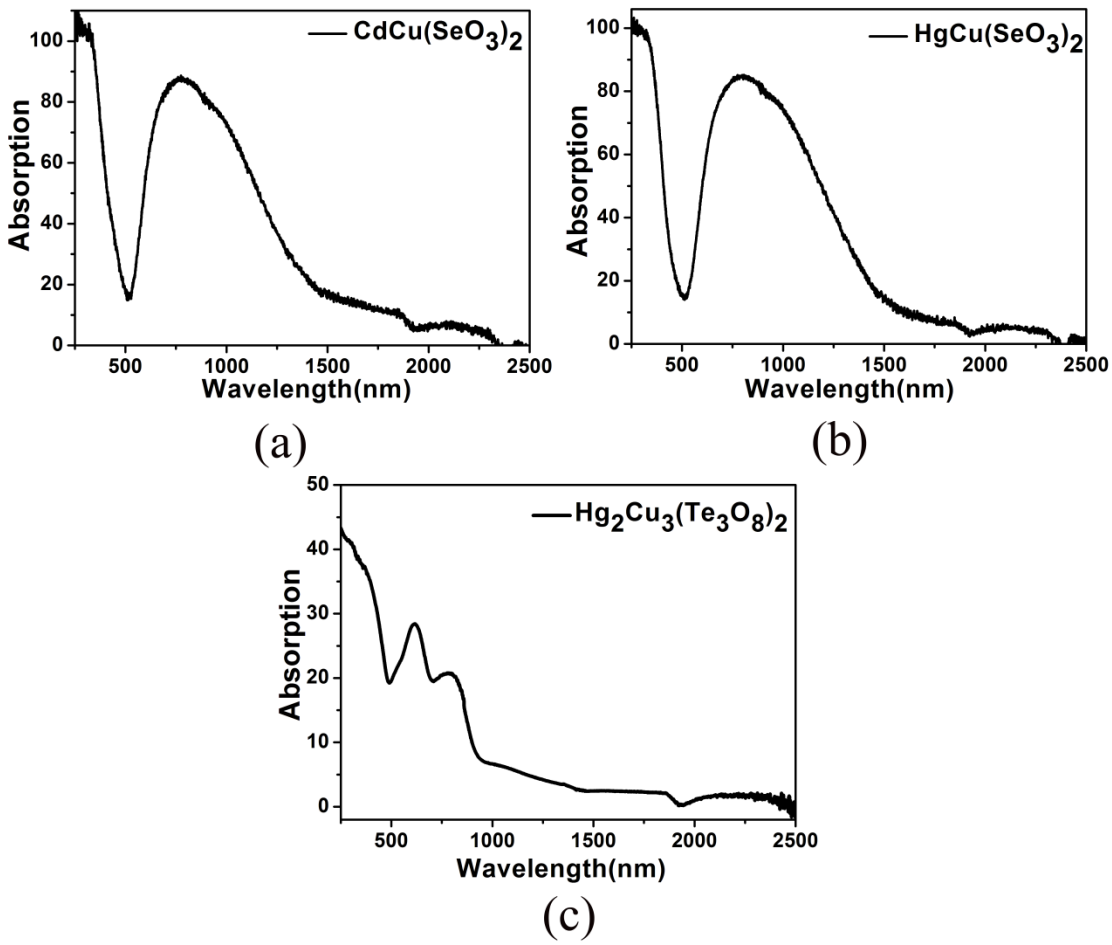

Figure S5. UV-Vis absorption spectra of $CdCu(SeO_3)_2$ (a), $HgCu(SeO_3)_2$ (b), and $Hg_2Cu_3(Te_3O_8)_2$ (c).

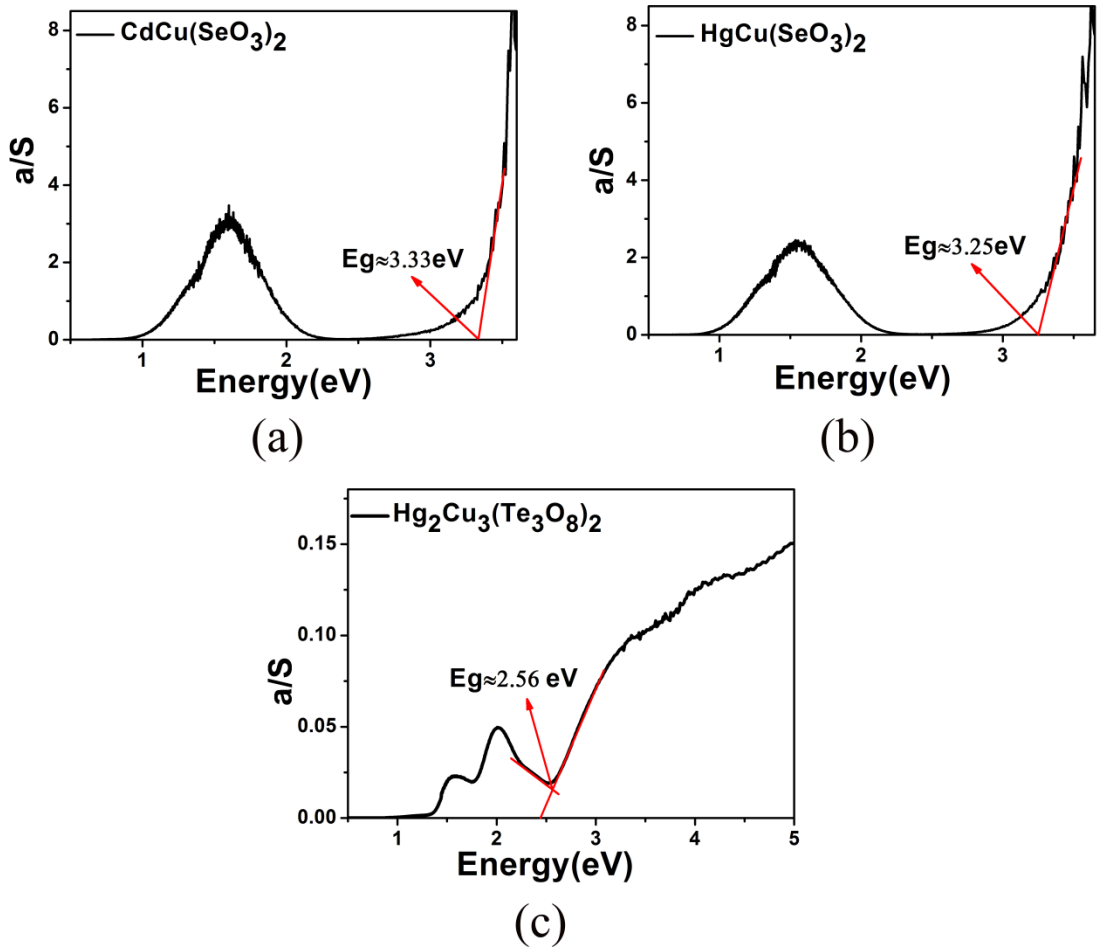

Figure S6. Optical diffuse reflectance spectra of $CdCu(SeO_3)_2$ (a), $HgCu(SeO_3)_2$ (b) and $Hg_2Cu_3(Te_3O_8)_2$ (c).

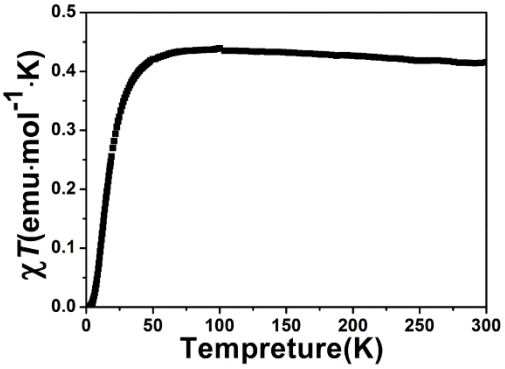

Figure S7. Plot of χT versus T for $HgCu(SeO_3)_2$.

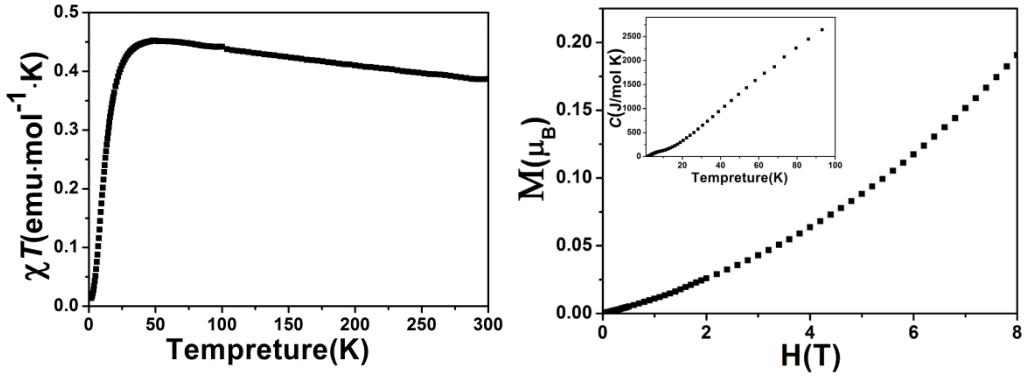

(a) (b)

Figure S8. Plot of χT versus T (a), and magnetization versus applied field at 2 K (b) as well as heat capacity measured in zero magnetic fields (the inset) for $CdCu(SeO_3)_2$.

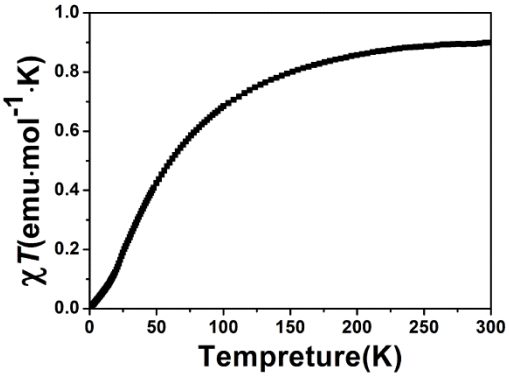

Figure S9. Plot of χT versus T for $Hg_2Cu_3(Te_3O_8)_2$.